

Article

# Growth Mechanism of Seed-Layer Free ZnSnO<sub>3</sub> Nanowires: Effect of Physical Parameters

Ana Rovisco <sup>\*</sup>, Rita Branquinho , Jorge Martins , Elvira Fortunato, Rodrigo Martins and Pedro Barquinha <sup>\*</sup>

i3N/CENIMAT, Department of Materials Science, Faculty of Science and Technology, Universidade NOVA de Lisboa and CEMOP/UNINOVA, Campus de Caparica, 2829-516 Caparica, Portugal

\* Correspondence: a.rovisco@campus.fct.unl.pt (A.R.); pmcb@fct.unl.pt (P.B.)

Received: 12 June 2019; Accepted: 9 July 2019; Published: 11 July 2019



**Abstract:** ZnSnO<sub>3</sub> semiconductor nanostructures have several applications as photocatalysis, gas sensors, and energy harvesting. However, due to its multicomponent nature, the synthesis is far more complex than its binary counter parts. The complexity increases even more when aiming for low-cost and low-temperature processes as in hydrothermal methods. Knowing in detail the influence of all the parameters involved in these processes is imperative, in order to properly control the synthesis to achieve the desired final product. Thus, this paper presents a study of the influence of the physical parameters involved in the hydrothermal synthesis of ZnSnO<sub>3</sub> nanowires, namely volume, reaction time, and process temperature. Based on this study a growth mechanism for the complex Zn:Sn:O system is proposed. Two zinc precursors, zinc chloride and zinc acetate, were studied, showing that although the growth mechanism is inherent to the material itself, the chemical reactions for different conditions need to be considered.

**Keywords:** nanowires; ZnSnO<sub>3</sub>; ZTO; hydrothermal synthesis; growth mechanism

## 1. Introduction

As a result of its impressive multifunctionality, ZnO-based thin films and nanostructures have received a lot of attention in the last 10 years [1–5]. While ZnO on its own captured a large interest, doping or mixing with other binary compounds brings a new level of possibilities, as the material properties can be improved/tailored to different applications depending on the cationic ratio. This has been widely explored in oxide thin films, with materials such as indium-gallium-zinc oxide (IGZO) [6–8] or with more sustainable approaches that avoid critical raw materials (In and Ga) [9], as zinc-tin oxide (ZTO) [10,11]. While in thin film form one of the major arguments of these multicomponent materials has been their amorphous structure, highly desirable for uniform large area electronics, when moving to nanostructure synthesis it is important to consider the different crystalline phases that are possible to achieve. ZTO structures crystallize by solid-state reaction in the stable inverse spinel ortho-stannate Zn<sub>2</sub>SnO<sub>4</sub> phase [12,13]. Nonetheless, it can also crystallize in metastable ZnSnO<sub>3</sub> phase, either in perovskite (orthorhombic, orth, or face centered, fcc) [14] or rhombohedral [15] forms. Both of these phases can result in nanostructures with different shapes and different properties, thus providing a large degree of multifunctionality with this material system [16–20]. Zn<sub>2</sub>SnO<sub>4</sub> is an n-type semiconductor with high mobilities in the order of 112 cm<sup>2</sup> V<sup>-1</sup> s<sup>-1</sup> and a reported band gap of 3.6 eV for nanostructures [21,22]. On the other hand, ZnSnO<sub>3</sub> is reported as having a high polarization along the z-axis of ~59 μC/cm<sup>2</sup>, which is much higher than that of ZnO (~5 μC/cm<sup>2</sup>) [18,23,24], and also as a ferroelectric material [19,25]. Its band gap of 3.9 eV is higher than that of Zn<sub>2</sub>SnO<sub>4</sub> [26,27]. Depending on the structure and phase ZTO nanostructures have been used for electronic [22,28–31] and energy harvesting [14,32–36] devices, catalysis [18,37–41], and sensors [42–44].

While vapor phase processes such as chemical vapor deposition (CVD) and thermal evaporation can be used to synthesize ZTO nanostructures with high efficiency [29,45], these expensive techniques are cumbersome and require high temperatures ( $>700$  °C). The demand for low-cost processes compatible with flexible substrates requires solution processes that allow for the synthesis of nanostructures at low cost, using simple and easy methods, ideally upscalable to industrial-scale quantities [46]. Recently, Shaodong et al. reviewed the different methods to fabricate ZTO nanostructures, showing the lack of well-controlled solution based methods to produce ZTO nanowires (NWs) of both  $\text{ZnSnO}_3$  and  $\text{Zn}_2\text{SnO}_4$  phases [12].

The multicomponent nature of ZTO makes the synthesis process quite challenging, given the different ionic sizes and diffusivity of the cations. Furthermore, each ZTO structure has different nucleation and growth times and requires a specific range of synthesis temperature [47]. For these reasons, a comprehensive study on the synthesis of ZTO nanostructures is needed. Studies on the influence of chemico-physical parameters on the hydrothermal synthesis of ZTO have been reported, showing the possibility to control the shape and type of the nanostructures and consequently the electrical, optical, and mechanical properties [13,48,49]. Recently, we reported a thorough description of the influence of different hydrothermal synthesis' chemical parameters in the growth of ZTO nanostructures [50]. This work was conducted without employing any seed-layer; hence, the obtained structures depend exclusively on the chemico-physical parameters of the synthesis. Moreover, the obtained nanostructures are produced in form of powder, which in conjunction with a variety of transfer methods, allow for a higher degree of freedom for integration on different substrates [51], without contamination from the seed-layer material [44]. In the last decade, the physical parameters of solution-based synthesis have also been studied showing that they have a large influence in the growth of the nanostructures. Zeng et al. reported the influence of temperature and time [49], showing that in order to achieve  $\text{Zn}_2\text{SnO}_4$  nanocrystals, a temperature of 200 °C and at least 20 h of reaction time are needed. Gou et al. studied the evolution of  $\text{ZnSnO}_3$ -orth nanoplates with the time and temperature of the synthesis, showing that producing these type of structures required 12 h at 260 °C, for that specific solution process [14]. These structures were applied to nanogenerators, in a composite with PDMS, resulting in a piezoelectric coefficient ( $d_{33}$ ) of 49 pC/N. This value is more than three times than the typically reported for ZnO nanostructures [52].

In this paper, the effect of the physical parameters on the hydrothermal synthesis of ZTO nanostructures, namely the influence of the volume of solution, temperature, and reaction time of the synthesis, is shown. In line with our previous work about the effect of the chemical conditions, this study is orientated towards the synthesis of ZTO nanowires, more specifically  $\text{ZnSnO}_3$ , which properties allow to envisage application on numerous next-generation nanoscale devices such as nanogenerators [35,36,53], sensors [54–56], photocatalysis [57], solar cells [58], resistive switching memories [59,60], and transistors [22,29]. Moreover, we have previously shown that the structures synthesized using this hydrothermal method have properties that are similar to those produced by expensive and high-temperature methods [50], thus, being promising materials for a new wave of multifunctional and low-cost devices.

## 2. Materials and Methods

### 2.1. Nanostructures' Synthesis

$\text{ZnSnO}_3$  nanowires were synthesized via hydrothermal method in a conventional oven, using the same methodologies and reagents reported previously by our group [50]. The most favorable chemical conditions to produce  $\text{ZnSnO}_3$  nanowires previously obtained in [50] using tin (IV) chloride 5-hydrate ( $\text{SnCl}_4 \cdot 5\text{H}_2\text{O}$ ) as tin precursor and both zinc chloride ( $\text{ZnCl}_2$ ) and zinc acetate ( $\text{Zn}(\text{CH}_3\text{COO})_2$ , ZnAc) as zinc precursors were maintained in this work. Briefly the ZTO hydrothermal synthesis was performed by dissolving the zinc (0.02 M/0.0657 g of ZnAc or 0.04 M/0.0818 g of  $\text{ZnCl}_2$ ) and tin (0.02 M/0.1050 g) precursors separately in 7.5 mL of deionized water and then mixed together, 7.5 mL of the surfactant

ethylenediamine (EDA) were then added and left stirring for 30 min, after which the mineralizer sodium hydroxide (NaOH, 0.24 M/0.1450 g) was added. The solution was then transferred into a 45 mL Teflon-lined stainless-steel autoclave (Parr Acid Digestion Bombs, no 4744, Moline, IL, USA), and kept in an electric oven (Thermo Scientific, Waltham, MA, USA) varying the temperature and the reaction time, using a heating ramp of 200 °C/h. Aiming to study the influence of the physical parameters in the ZTO nanostructures growth, we varied the mixture volume (7.5 mL, 11 mL, and 15 mL), the synthesis temperature (150 °C, 180 °C, 200 °C, and 220 °C), and reaction time (2 h, 8 h, 12 h, 18 h, 24 h, 36 h, and 48 h). After the synthesis time, the autoclave was cooled to ambient temperature, naturally. The final product (white precipitate) comprising the nanostructures, was alternately washed with deionized water and isopropyl alcohol (at least 5 times) and centrifuged at 4000 rpm. After washed, the nanostructures were dried at 60 °C, in vacuum, for 2 h. As was previously reported [50], the syntheses present a good reproducibility, especially when using ZnCl<sub>2</sub> due its better solubility in ethylenediamine.

## 2.2. Nanostructures' Characterization

All the nanostructures' characterization was performed with the synthesis product in powder form. In order to study the morphology and elemental composition of the nanostructures, scanning electron microscopy (SEM) and energy dispersive X-ray spectroscopy (EDS) inside an AURIGA CrossBeam workstation were performed (Zeiss, Oberkochen, Germany). The structural characterization was carried out by X-Ray diffraction (XRD) using X'Pert PRO MRD diffractometer (PANalytical, Royston, UK) with Cu K $\alpha$  radiation and the data acquisition range was 10–90° (2 $\theta$ ) with a step size of 0.033°. Fourier-transform infrared (FTIR) spectra were acquired in the range of 4000–525 cm<sup>-1</sup> with 4 cm<sup>-1</sup> resolution and 45° incident angle. The data was recorded using a Smart iTR attenuated total reflectance (ATR) sampling accessory (Thermo Scientific, Waltham, MA, USA) equipped with a single bounce diamond crystal on a Thermo Nicolet 6700 Spectrometer (Thermo Scientific, Waltham, MA, USA). Raman spectra were acquired using an inVia Reflex micro-Raman spectrometer (Renishaw, Wotton-under-Edge, UK) equipped with an air-cooled CCD detector and a HeNe laser using a 532 nm laser excitation with a power of 50 mW, with 0.3 cm<sup>-1</sup> resolution. All measurements were obtained with an intensity of 50  $\mu$ W at room temperature in a range of 100–1600 nm, using an integration time of 2 scans (10 s each).

## 3. Results and Discussion

### 3.1. Reaction Mixture Volume

A hydrothermal process is a method to produce single and polycrystalline structures, in aqueous solution at high temperature and high pressure. Both reaction mixture volume and temperature are determinant to the pressure inside the autoclave, consequently defining the growth of the nanocrystals. However, the phase transformation mechanism that occurs in polymorphs materials under high pressure is not completely controlled and understood [61].

In order to study the influence of the pressure caused by the solution's volume in the ZnSnO<sub>3</sub> nanowires growth in this specific hydrothermal method, volumes of 7.5 mL, 11 mL, and 15 mL were tested, representing 17%, 24%, and 33% of the autoclave volume, respectively. The temperature was fixed at 200 °C and the reaction time was 24 h.

In general, a mixture of ZnO nanowires, SnO<sub>2</sub> nanoparticles, and Zn<sub>2</sub>SnO<sub>4</sub> nanostructures can be found in these syntheses, still with the increasing of the mixture volume mainly ZnSnO<sub>3</sub> nanowires are obtained. Figure 1a shows small differences in the XRD pattern for the different volumes when using the ZnCl<sub>2</sub> precursor. The most significant difference is the peak at 32° appearing for the volumes of 11 and 15 mL, attributed to ZnO phase. Raman analysis (Figure S1a) shows an intense peak at 437 cm<sup>-1</sup>, characteristic of ZnO [62], being this peak more intense for 11 mL, in agreement with the XRD data. The SEM images in Figure 2 clearly show that less volume gives rise to smaller nanowires. As

we previously identified in Reference [50], when a volume of 15 mL was used, these nanowires have the  $\text{ZnSnO}_3$  orthorhombic perovskite phase, represented by the card 00-028-1486. Even if this card has been used before in several reports [63–66], it was deleted from ICDD database due to matching peaks with the mixture of  $\text{SnO}_2$  and  $\text{Zn}_2\text{SnO}_4$ . Although in 00-028-1486 card the peak with most intensity is at  $26^\circ$ , this peak corresponds to the 012 plane, which is not the preferential orientation of the nanowires when measured in XRD. In order to confirm the  $\text{ZnSnO}_3$  identification, we performed peak indexing in different samples, which always showed matching to an orthorhombic phase characteristic of  $\text{ZnSnO}_3$  and not of  $\text{Zn}_2\text{SnO}_4$  and  $\text{SnO}_2$  mixture. EDS analysis confirms the 1:1 Zn:Sn ratio of the nanowires (Figure S2), reinforcing the hypothesis of the  $\text{ZnSnO}_3$  phase. Nevertheless, Raman analysis suggests that both  $\text{ZnSnO}_3$  and  $\text{Zn}_2\text{SnO}_4$  should be present in the sample, given the characteristic peaks identified at  $538\text{ cm}^{-1}$  and  $676\text{ cm}^{-1}$  [49].

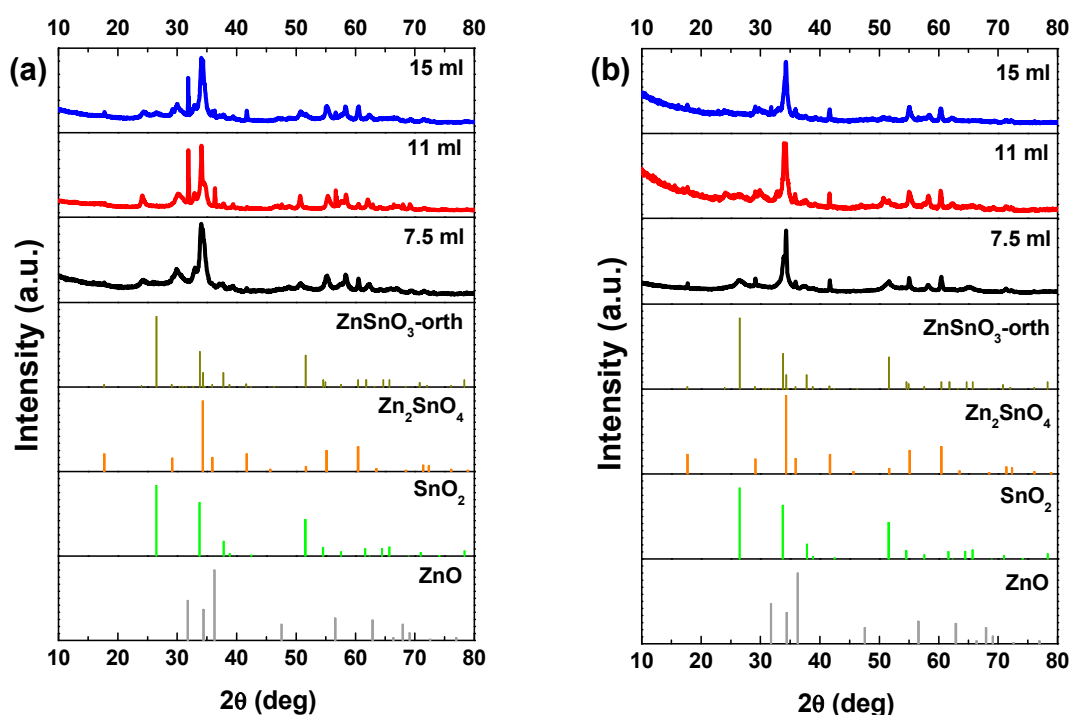


**Figure 1.** XRD patterns when using (a)  $\text{ZnCl}_2$  precursor (with 2:1 Zn:Sn ratio) and (b)  $\text{ZnAc}$  precursor (with 1:1 Zn:Sn ratio), for different solution mixture volumes (7.5 mL, 11 mL, and 15 mL). Identification following ICDD card 00-028-1486 ( $\text{ZnSnO}_3$ -orth, deleted), 00-024-1470 ( $\text{Zn}_2\text{SnO}_4$ ), 01-077-0452 ( $\text{SnO}_2$ ), and 00-06-1451 ( $\text{ZnO}$ ).

When  $\text{ZnAc}$  is used as the zinc source the presence of  $\text{ZnO}$  is partially or even completely suppressed. Similar to the results obtained using  $\text{ZnCl}_2$ , longer  $\text{ZnSnO}_3$  nanowires are obtained for higher volumes of solution mixture. While for the lower volume (7.5 mL)  $\text{Zn}_2\text{SnO}_4$  is the predominant phase, for 11 mL,  $\text{ZnSnO}_3$  nanowires are predominant, although some  $\text{Zn}_2\text{SnO}_4$  nanostructures are also observed (Figure S3) and ultimately for 15 mL,  $\text{ZnSnO}_3$  nanowires are the predominant structures.  $\text{SnO}_2$  can also be identified by XRD (Figure 1b), even if it is not clear by Raman (Figure S1b) for all the conditions. The presence of residual  $\text{ZnO}/\text{SnO}_2$  for synthesis using the  $\text{ZnCl}_2/\text{ZnAc}$  precursors, is attributed to the Zn precursor's higher/lower solubility in ethylenediamine when compared to the  $\text{SnCl}_4 \cdot 5\text{H}_2\text{O}$ , leading to an earlier availability of Zn/Sn species in the synthesis [50].

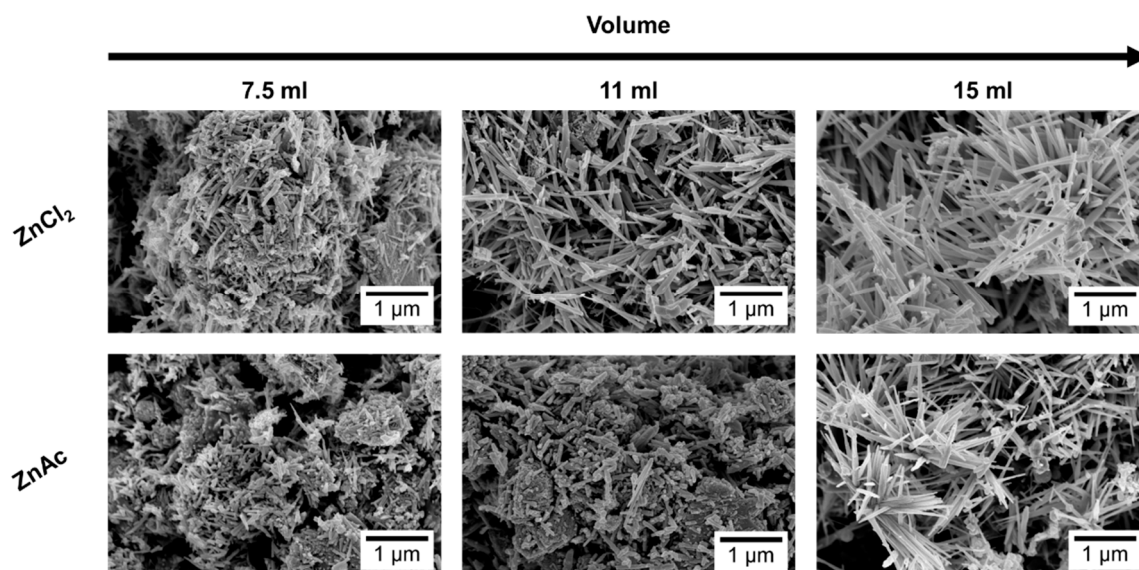
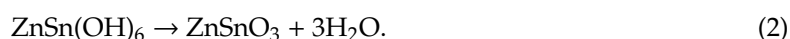
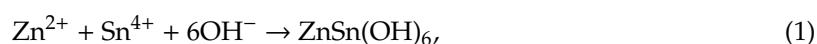


**Figure 2.** SEM images of nanostructures obtained for different reaction mixture volumes, 7.5 mL, 11 mL, and 15 mL, using ZnCl<sub>2</sub> and ZnAc as zinc precursor.

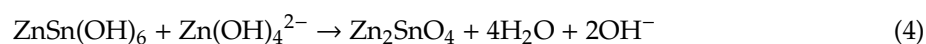
Nakayama et al. reported a theoretical study where the relation between the enthalpy and pressure for the system Zn–Sn–O was investigated [23]. They showed that the global energy minimum corresponds to the mixed phases Zn<sub>2</sub>SnO<sub>4</sub> and SnO<sub>2</sub>. Our experimental results are in agreement with this study, as for lower volume and consequently lower pressure, the formation of Zn<sub>2</sub>SnO<sub>4</sub> and SnO<sub>2</sub> nanoparticles is favored, although mixed with ZnSnO<sub>3</sub> nanowires. Moreover, in 2010 Gou et al. also reported a theoretical study about the ZnSnO<sub>3</sub> phase transition under pressure [61]. According to the authors the ZnSnO<sub>3</sub> synthesis at low-temperature (<700 °C) is unfavorable, leading to a mixture of phases, mainly due to its positive formation enthalpies. This decomposition has also been reported to occur at temperature above 500 °C [13,67]. Taking into account the temperature used in this study (200 °C), our results are in fair agreement with this, since with decreasing volume, and consequently pressure, the trend is to achieve higher mixture of phases while the more homogeneous ZnSnO<sub>3</sub> nanowires are obtained when using the higher solution volume, 15 mL. The high pressure inside the autoclave, characteristic of a hydrothermal method, supplies high energy levels to the reaction, leading to an acceleration of the nucleation processes at even lower temperatures. For the reasons explained, 15 mL was the volume used for both precursors for the next studies presented here.

### 3.2. Synthesis Temperature

To understand the growth mechanisms of ZTO nanostructures, one needs to have in mind the chemical reaction processes. Based on different reports, the ZnSnO<sub>3</sub> nanostructures formation follows the equations below [14,63,68]:



Regarding Zn<sub>2</sub>SnO<sub>4</sub>, its formation can be represented by the following equations together with Equation (1):



ZnSnO<sub>3</sub> can have the fcc or the orthorhombic structures, and these two different structures present different heat of formation and total energies. Gou et al. presented these values for the different possible structures of ZnSnO<sub>3</sub> [61]. On the other hand, it is already well-known that the ZnSnO<sub>3</sub> phase is metastable [12,13] and according, for example, to the study reported by Bora et al. this phase suffers a decomposition into the thermodynamically stable phases Zn<sub>2</sub>SnO<sub>4</sub> and SnO<sub>2</sub> at temperatures higher than 500 °C [67]. This decomposition can be represented by the following equation:



However, it is clear that above atmospheric pressure, as in the case of the hydrothermal method, and depending of the reaction mixture, the temperature at which the decomposition occurs can change.

In order to investigate the effect of temperature in the specific conditions of our syntheses, four different temperatures were used: 150 °C, 180 °C, 200 °C, and 220 °C, while maintaining all the other conditions and keeping the volume of the solution mixture at 15 mL.

SEM images, in Figure 3, show that at 150 °C, mainly nanoparticles are obtained. In the XRD pattern (Figure 4) a mixture of phases (ZnSn(OH)<sub>6</sub> and Zn<sub>2</sub>SnO<sub>4</sub> and/or ZnSnO<sub>3</sub>) can be observed using ZnCl<sub>2</sub>, while when using ZnAc, only Zn<sub>2</sub>SnO<sub>4</sub> is identified. Raman analysis (Figure S4) is in agreement with these results, showing the peak at 603 cm<sup>-1</sup>, characteristic of ZnSn(OH)<sub>6</sub> (only for ZnCl<sub>2</sub>) and the characteristics peaks of ZTO for both Zn sources (538 cm<sup>-1</sup> and 676 cm<sup>-1</sup>). It is important to refer that the 603 cm<sup>-1</sup> vibrational band is not only a characteristic peak of ZnSn(OH)<sub>6</sub>, but also of fcc-ZnSnO<sub>3</sub> [67] that could also be present in these samples. However, FTIR analysis supports the ZnSn(OH)<sub>6</sub> hypothesis by showing OH<sup>-</sup> groups for wavenumbers above 3000 cm<sup>-1</sup> (Figure S5a), corresponding to ZnSn(OH)<sub>6</sub>. In EDS analysis, shown in Figure S6, it can be seen that the nanoparticles obtained using ZnAc have the Zn:Sn ratio of 2:1 corresponding to the Zn<sub>2</sub>SnO<sub>4</sub> phase.

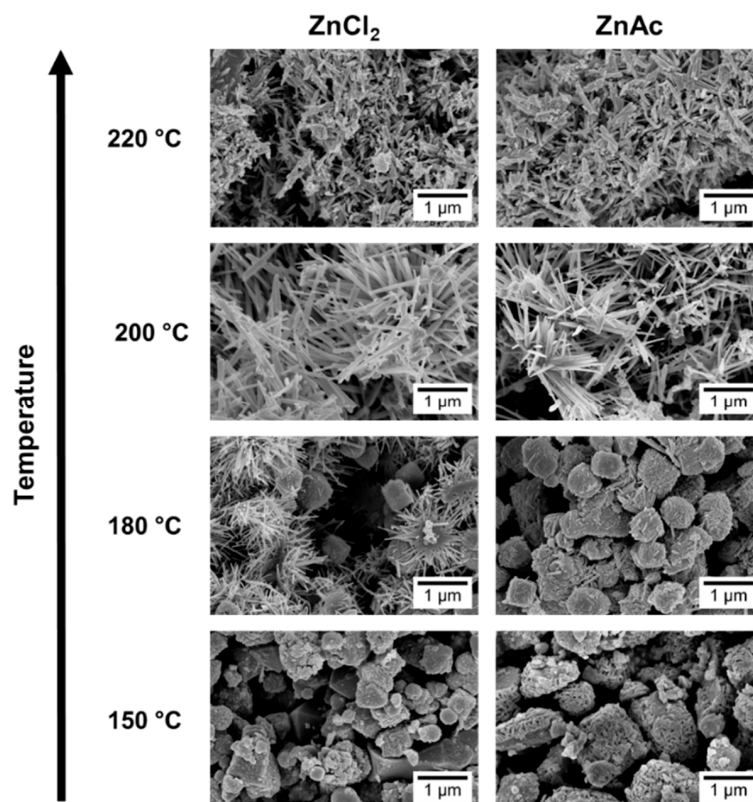


**Figure 3.** SEM images of the nanostructures obtained using the previous best conditions (15 mL) for each zinc precursor (ZnCl<sub>2</sub> and ZnAc) at different temperatures: 150 °C, 180 °C, 200 °C, and 220 °C.

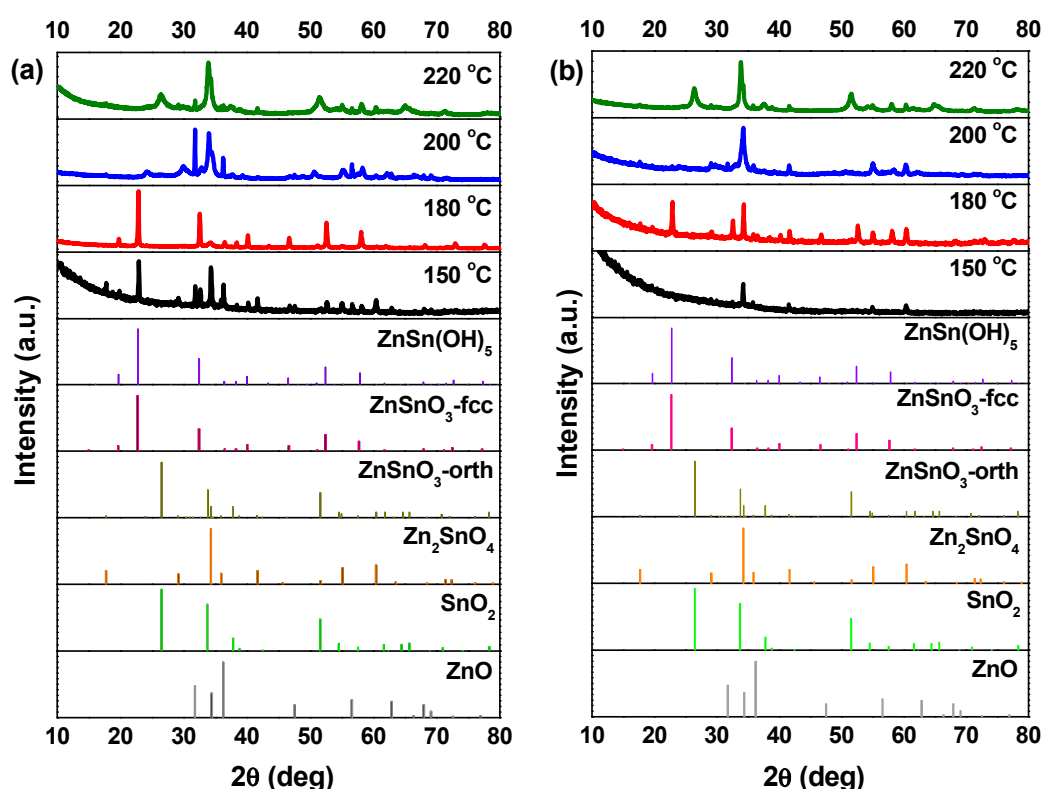


**Figure 4.** XRD patterns when using (a)  $\text{ZnCl}_2$  precursor (with 2:1 Zn:Sn ratio) and (b)  $\text{ZnAc}$  precursor (with 1:1 Zn:Sn ratio), at different temperatures: 150 °C, 180 °C, 200 °C, and 220 °C. Identification following ICDD card 00-028-1486 ( $\text{ZnSnO}_3$ -orth—deleted), 00-011-0274 ( $\text{ZnSnO}_3$ -fcc), 00-024-1470 ( $\text{Zn}_2\text{SnO}_4$ ), 01-077-0452 ( $\text{SnO}_2$ ), and 00-06-1451 ( $\text{ZnO}$ ).

Increasing the temperature to 180 °C, some nanowires can be viewed in SEM when using the  $\text{ZnCl}_2$  precursor (Figure 3), which can be  $\text{ZnSnO}_3$  according to the XRD (Figure 4a). Still, at this temperature,  $\text{OH}^-$  groups are very evident from the FTIR analysis (Figure S5a) for both zinc precursors, with XRD showing predominantly the  $\text{ZnSn(OH)}_6$  phase, an intermediate stage of the  $\text{ZnSnO}_3$  formation. Zeng et al. also showed that for temperatures lower than 200 °C  $\text{ZnSn(OH)}_6$  is the predominant phase [49]. Nevertheless, XRD also shows that other phases are present (Figure 4). In fact, EDS (Figure S7) and Raman (Figure S4) confirm this by showing a reasonable amount of  $\text{Zn}_2\text{SnO}_4$  octahedrons, especially when using  $\text{ZnAc}$  as precursor. It means that, as already discussed, at these lower temperatures, and consequently lower pressures, the formation of the thermodynamically more stable  $\text{Zn}_2\text{SnO}_4$  nanoparticles is promoted. The lower solubility of  $\text{ZnAc}$  in ethylenediamine, when compared to  $\text{ZnCl}_2$ , can explain why a higher mixture of phases is seen for this case.

Moreover, in Figure S5a,b, FTIR spectra of both precursors for 150 °C and 180 °C presents several peaks in the range of 1250 to 500  $\text{cm}^{-1}$ . The origin of these peaks can be associated to residual reagents in the final product (see Figure S8 in supporting information) [69], which means that when using temperatures lower than 200 °C, the reagents are not completely consumed. An exception is seen for synthesis at 150 °C using  $\text{ZnAc}$ , where these peaks are not present and  $\text{Zn}_2\text{SnO}_4$  nanoparticles were obtained, as these are the more stable ZTO nanostructures.

The samples at 200 °C were already described in the previous section and result mainly in  $\text{ZnSnO}_3$  nanowires. For this temperature, as seen in Figure S5, FTIR analysis confirms that no  $\text{OH}^-$  groups are present, meaning that the intermediate phase  $\text{ZnSn(OH)}_6$  is no longer obtained at this temperature. It should be added that FTIR also shows that all the reagents were completely consumed.

Increasing the temperature to 220 °C leads to the formation of  $\text{SnO}_2$  and  $\text{Zn}_2\text{SnO}_4$  phases, even if the  $\text{ZnSnO}_3$  nanowires are still predominant. While it is not evident in the XRD pattern, through

Raman analysis (Figure S4) their presence is clear since it is possible to observe the  $631\text{ cm}^{-1}$  and  $538\text{ cm}^{-1}$  peaks, characteristic of Sn–O and M–O tetrahedrons bonds, respectively. This result is attributed to the decomposition of  $\text{ZnSnO}_3$  into  $\text{SnO}_2$  and  $\text{Zn}_2\text{SnO}_4$ , due to its metastability. This decomposition has been reported to occur at temperatures above  $500\text{ }^\circ\text{C}$  [13,61,67]. In the present study, this decomposition occurs at lower temperature due to the high energy levels inherent to the hydrothermal process (high temperature and pressure).

In conclusion, it is clear that for temperatures lower than  $200\text{ }^\circ\text{C}$ , homogeneous nanowires are not produced as, in accordance to what was observed in the previous section, for lower available energy, the formation of  $\text{ZnSnO}_3$  is not feasible, and instead the more stable phase  $\text{Zn}_2\text{SnO}_4$  is favored (along with the intermediate phase  $\text{ZnSn}(\text{OH})_6$ ). Meanwhile, for temperatures around  $200\text{ }^\circ\text{C}$ , almost only  $\text{ZnSnO}_3$  nanowires are produced. For higher temperatures ( $220\text{ }^\circ\text{C}$ ), no improvements are observed in terms of producing only nanowires, as decomposition of those into the more stable phases starts to occur. This study shows that the temperature to achieve the desired structures must be carefully considered, as it should be high enough to allow the formation of the metastable phase, but not too high to promote the decomposition process.

### 3.3. Reaction Time

Throughout the reaction time of the synthesis, the ZTO nanostructures undergo a complex evolution. Thus, a careful investigation on the evolution of ZTO morphology and crystallinity was performed for different reaction times (2 h, 8 h, 12 h, 18 h, 24 h, 36 h, and 48 h), for both zinc precursors ( $\text{ZnCl}_2$  and  $\text{ZnAc}$ ) and using the most favorable conditions as defined in the previous sections (15 mL of volume at  $200\text{ }^\circ\text{C}$ ).

Similar to what was observed with the study of the effect of the temperature,  $\text{ZnSn}(\text{OH})_6$  appears as an intermediate phase before the formation of the  $\text{ZnSnO}_3$  or the  $\text{Zn}_2\text{SnO}_4$  phases (represented by Equations (1)–(4)).

In Figure 5a,b, the XRD patterns for the structures from synthesis with different reaction times are shown. For 2 h of synthesis,  $\text{ZnSn}(\text{OH})_6$  can be identified, for both zinc precursors. As already mentioned, this phase can be mistaken with fcc- $\text{ZnSnO}_3$  in XRD pattern and also in Raman analysis (Figure S9) where an intense peak at  $603\text{ cm}^{-1}$  is evident. Nonetheless, FTIR analysis in Figure S10 clarifies this by showing the presence of  $\text{OH}^-$  groups, confirming the presence of  $\text{ZnSn}(\text{OH})_6$ . Although  $\text{ZnSn}(\text{OH})_6$  phase is predominant for both Zn sources, when using  $\text{ZnAc}$ , it is also possible to identify  $\text{Zn}_2\text{SnO}_4$  by XRD, and when using  $\text{ZnCl}_2$ , Raman analysis indicates  $\text{ZnSnO}_3$  and/or  $\text{Zn}_2\text{SnO}_4$  may be present.

When using  $\text{ZnCl}_2$ , the  $\text{ZnSn}(\text{OH})_6$  phase appears for synthesis of 2 h, while for synthesis of 8 h or longer, neither  $\text{OH}^-$  groups (from the intermediate phase  $\text{ZnSn}(\text{OH})_6$ ) nor leftover precursors are observed in FTIR spectra (Figure S10), unlike when using  $\text{ZnAc}$ , where these are present up to 8 h of synthesis. For 8 h of synthesis, while the nanoparticles are still predominant, some orthorhombic  $\text{ZnSnO}_3$  nanowires start to be present and, from this reaction time onwards, these nanowires are the predominant structure achieved, with both precursors.

Regarding the use of the  $\text{ZnCl}_2$ , a particular case is observed for the 12 h long synthesis. In this condition,  $\text{ZnSnO}_3$ -fcc also seems to be obtained, mixed with  $\text{ZnSnO}_3$ -orth. The possibility to obtain this type of structures for lower energies was already demonstrated as it is an intermediate phase between  $\text{ZnSn}(\text{OH})_6$  and  $\text{ZnSnO}_3$ -orth [61]. Also, it is relevant to consider the possibility of formation of  $\text{Zn}(\text{OH})_2$  due to the presence of  $\text{Zn}(\text{OH})_4^{2+}$ , which is an intermediate phase of formation of both  $\text{Zn}_2\text{SnO}_4$  and  $\text{ZnO}$ . In XRD, the phase  $\text{Zn}(\text{OH})_2$  (that is transformed in  $\text{Zn}(\text{OH})_4^{2+}$ ) can be mistaken with hexagonal phase  $\text{ZnO}$ . Also, in EDS mapping (shown in Figure S11), it is possible to observe some nanoparticles with a large Zn signal, that can be attributed either to  $\text{Zn}(\text{OH})_2$  or to  $\text{Zn}_2\text{SnO}_4$ . As such, the possibility of having  $\text{Zn}(\text{OH})_2$  cannot be discarded. This emphasizes the difficulty of obtaining only one phase and one type of ZTO nanostructure using a solution-based method and the demand for a well-controlled synthesis process.

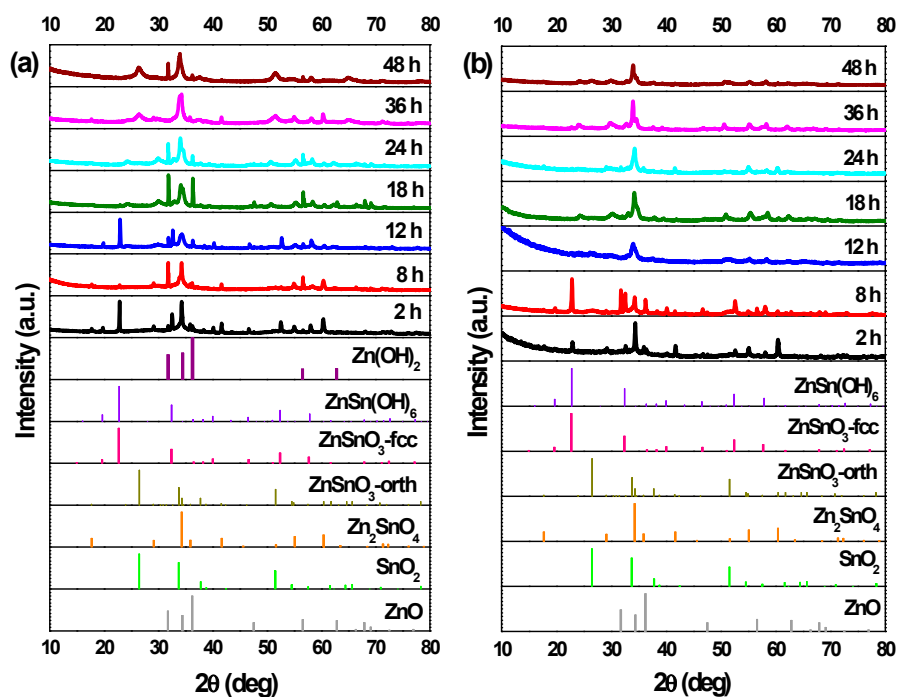


**Figure 5.** XRD patterns when using (a)  $\text{ZnCl}_2$  precursor (with 2:1 Zn:Sn ratio) and (b) ZnAc precursor (with 1:1 Zn:Sn ratio), for different reaction time: 2 h, 8 h, 12 h, 18 h, 24 h, 36 h, and 48 h. Syntheses at  $200^\circ\text{C}$ , using 15 mL of reaction mixture volume. Identification following ICDD cards: 00-028-1486 ( $\text{ZnSnO}_3$ -orth—deleted), 00-011-0274 ( $\text{ZnSnO}_3$ -fcc), 00-024-1470 ( $\text{Zn}_2\text{SnO}_4$ ), 01-077-0452 ( $\text{SnO}_2$ ), 00-06-1451 ( $\text{ZnO}$ ), and 00-048-1066 ( $\text{Zn(OH)}_2$ ).

In the case of using the ZnAc precursor, for synthesis of 12 h or longer, the XRD pattern (Figure 5a) seems to be similar (evidencing  $\text{ZnSnO}_3$  nanowires) with a higher crystallinity for the longer synthesis when compared to 12 h. SEM images (Figure 6) show that longer nanowires are obtained for 36 h or 48 h long synthesis. Table 1 shows the lengths of the nanowires for both precursors, emphasizing this observation. On the other hand, when using  $\text{ZnCl}_2$ , while nanowires' lengths increase up to around 18 h or 24 h, these start to significantly decrease for longer synthesis (Figure 6, Table 1). It can be observed through XRD data (Figure 5) that when synthesis is 36 h or longer,  $\text{ZnSnO}_3$  phase transformation into  $\text{Zn}_2\text{SnO}_4$  and  $\text{SnO}_2$  starts to occur, in a similar trend to that seen in the previous section for the increase of temperature beyond  $200^\circ\text{C}$ , causing the diminishing of the nanowires' length.

**Table 1.** Evolution of the average of nanowires' length with the reaction time.

Reaction Time (h)	Nanowires' Length (nm)	
	$\text{ZnCl}_2$	ZnAc
24	$605 \pm 75$	$540 \pm 175$
36	$420 \pm 115$	$1090 \pm 250$
48	$220 \pm 35$	$950 \pm 190$

It can be induced that, due to the  $\text{ZnCl}_2$ 's higher solubility in ethylenediamine, the evolution of the phases happens faster when this precursor is used. While for  $\text{ZnCl}_2$ , a phase transformation of  $\text{ZnSnO}_3$  to  $\text{Zn}_2\text{SnO}_4$  and  $\text{SnO}_2$  starts to occur at 36 h, for ZnAc, a pronounced length increase is still observed up to 36 h, supporting the assumption that a slower reaction is taking place when using ZnAc precursor. While this results in an increased synthesis time to achieve longer nanowires, these are significantly longer (more than 2x) than when using  $\text{ZnCl}_2$ . Nevertheless, for 48 h, there is a small deterioration in terms of nanowire length and homogeneity of the nanostructures' phases, thus 36 h is the optimal reaction time for the conditions studied.

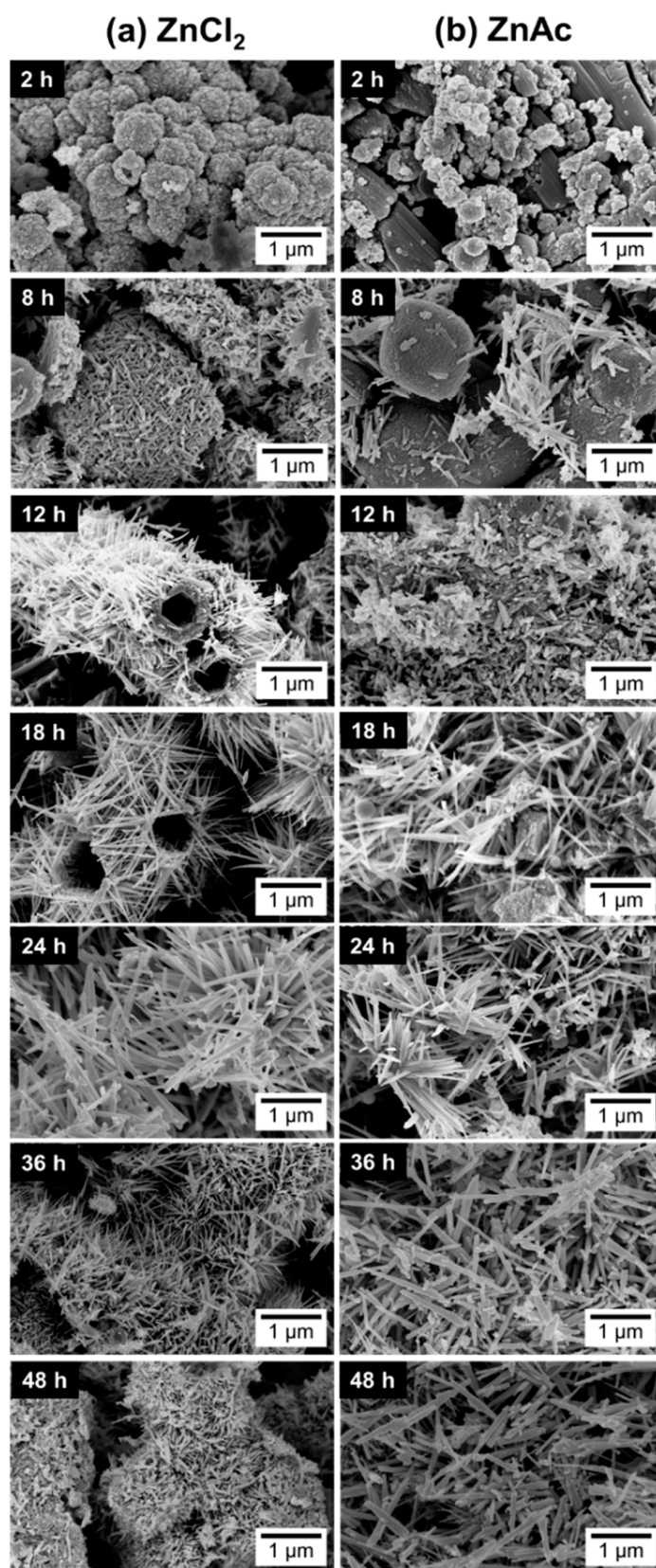


**Figure 6.** SEM images of the nanostructures obtained by synthesis using ZnCl<sub>2</sub> (a) and ZnAc (b) with different reaction time, showing the temporal evolution of the structures produced. Syntheses at 200 °C, using 15 mL of reaction mixture volume.

In summary, in Figure 6, one can clearly visualize the large dependency of the nanostructures' growth with the increase of reaction time. For both precursors, it is clear that at least 12 h are necessary to start producing predominantly  $\text{ZnSnO}_3$  nanowires, being that only after 24 h this production starts being homogeneous. It is also possible to observe that, similarly to what was concluded with previous studies on the influence of the chemical parameters [50], the ZTO nanostructures obtained using ZnAc are generally smaller than those obtained using  $\text{ZnCl}_2$ , for synthesis up to 24 h. When using ZnAc, the ZTO growth is slower so the higher dimensions are obtained for longer reaction times (36 h and 48 h), for which the nanowires reach higher dimensions than that those obtained with  $\text{ZnCl}_2$ . This difference in the optimal reaction time can be attributed to the lower solubility of ZnAc when compared with  $\text{ZnCl}_2$  in the solvent ethylenediamine. This also leads to a constant presence of  $\text{SnO}_2$  for the syntheses with ZnAc, while when using  $\text{ZnCl}_2$ , ZnO is constantly observed. This study shows that if longer nanowires are desired, ZnAc is the most suitable precursor, while if faster processing is desired, the most suitable precursor is  $\text{ZnCl}_2$ .

### 3.4. Growth Mechanism of $\text{ZnSnO}_3$ Nanowires

Throughout the reaction time one of the main challenges in nanomaterials synthesis is to understand how the nanostructures grow, i.e., what are the mechanisms behind the formation of each phase and of each type of nanostructures. Obtaining only one phase and one shape is not an easy task, particularly for the Zn:Sn:O system due to its ternary composition, as evident throughout this manuscript. In the specific case of  $\text{ZnSnO}_3$  nanowires formation, the metastability of this phase adds even more complexity into understanding it properly. Gou et al. showed the influence of pressure and temperature in the enthalpy energy of different ZTO phases, including  $\text{ZnSnO}_3$  cubic perovskite, concluding that the formation of this phase is not favorable under ambient conditions and can only be obtained under high pressure and temperature [61]. However, under those conditions, this phase tends to decompose into  $\text{Zn}_2\text{SnO}_4$  and  $\text{SnO}_2$  [70]. Therefore, a very specific tailoring of the synthesis parameters is necessary when aiming to achieve proper structures of this metastable phase.

Owing to the careful optimization of the chemico-physical parameters performed here, it is possible to observe an evolution of the nanostructures, and its respective phase, with the increase of reaction time and increase of total energy available in the reaction. Although the aim was to achieve  $\text{ZnSnO}_3$  nanowires,  $\text{Zn}_2\text{SnO}_4$  nanostructures were also obtained, mainly for very short synthesis or for synthesis with lower temperatures or volumes, showing that this phase is achieved with lower available energy. These trends are represented in the Figure 7.

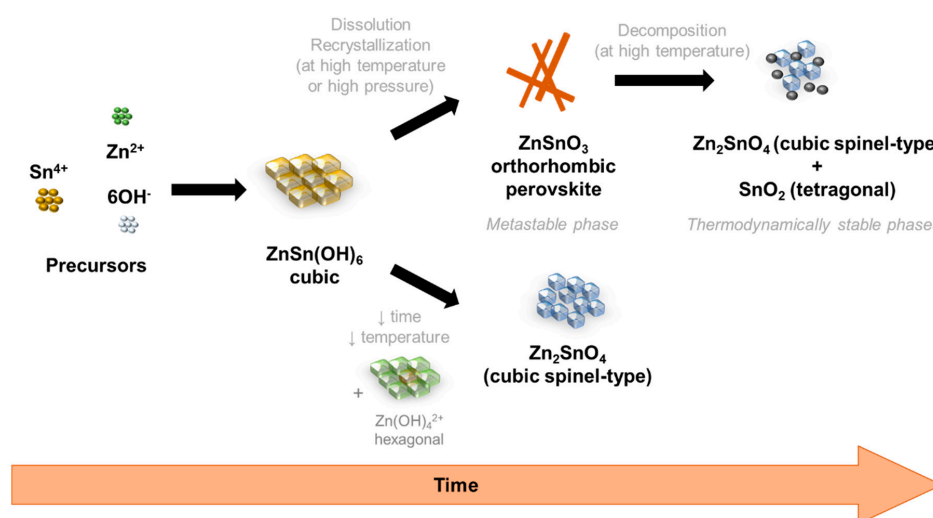


**Figure 7.** Schematic representation of the phase transformations on the hydrothermal synthesis of zinc-tin oxide (ZTO) nanostructures, depending on the energy available in the reaction and the time of synthesis.

#### 4. Conclusions

Due to its complexity, the synthesis of multicomponent oxide nanostructures requires an appropriate understanding of the influence of each synthesis' parameters and the growth mechanism itself. In this work, a detailed study on the influence of physical parameters on the hydrothermal synthesis of ZnSnO<sub>3</sub> nanowires is reported. Specifically, the effect of reaction mixture volume, synthesis temperature and reaction time were studied. The available energy in the reaction revealed to be one of the determinant factors on the final products. As already reported in the literature, the metastable ZnSnO<sub>3</sub> requires high pressures/energy conditions to be obtained. It was found that independently of the Zn source, ZTO nanostructures had the same time-dependence growth mechanisms, although with different time spans.

While previous reports have shown the degradation of the metastable ZnSnO<sub>3</sub> structures at temperatures above 500 °C, the present work demonstrates that owing to the high energy of the hydrothermal process, this decomposition can occur at considerably lower temperatures (24 h at 220 °C) and/or longer reaction times (36 h at 200 °C). This highlights the advantages of hydrothermal processes to obtain metastable multicomponent nanostructures such as ZnSnO<sub>3</sub> at low temperatures but also the importance of properly controlling and understanding all the synthesis parameters to achieve the desired structures. With ZnSnO<sub>3</sub> finding application as a piezoelectric material, catalyst, active material in gas sensors, resistive switching memories, batteries, and others, we expected this work to have a significant impact in the future of nanotechnology as it describes the synthesis of ZnSnO<sub>3</sub> nanowires without either direct growth in substrates or production by vapor phase methods (high temperatures). This new approach brings higher flexibility to the different applications, allowing a higher degree of freedom for integration on different substrates while avoiding contamination from the seed-layer material.

**Supplementary Materials:** The following are available online at <http://www.mdpi.com/2079-4991/9/7/1002/s1>, Figures S1, S4, and S9: Raman spectroscopy of the samples related to the studies of volume, temperature, and reaction time, respectively. Figures S2, S3, S6, S7, and S11: SEM images and EDS element analysis, which is used to assist in phases identification of each structure. Figures S5, S8, and S10: FTIR reaction time, synthesis temperature, and all reagents used in the syntheses, respectively.

**Author Contributions:** Experiments designed, and fabrication/characterization of the nanowires, A.R.; data analysis and manuscript preparation, A.R. and J.M.; supervision of the work and revision of the concept, structure, and content of the different versions of the manuscript until its final form, P.B. and R.B.; funding for the fabrication and characterization facilities and reviewed the final versions of the manuscript, R.M., E.F., and P.B.

**Funding:** This work is funded by National Funds through FCT - Portuguese Foundation for Science and Technology, Reference UID/CTM/50025/2019 and FCT/MCTES, as well as the doctoral grants research numbers SFRH/BD/131836/2017 and SFRH/BD/122286/2016. This work also received funding from the European Community's H2020 program under grant agreement No. 716510 (ERC-2016-STG TREND) and No. 685758 (1D-Neon).

**Conflicts of Interest:** The authors declare no conflict of interest.

#### References

1. Schmidt-Mende, L.; MacManus-Driscoll, J.L. ZnO—Nanostructures, defects, and devices. *Mater. Today* **2007**, *10*, 40–48. [[CrossRef](#)]
2. Kołodziejczak-Radzimska, A.; Jesionowski, T. Zinc Oxide—From synthesis to application: A review. *Materials* **2014**, *7*, 2833–2881. [[CrossRef](#)] [[PubMed](#)]
3. Pimentel, A.; Rodrigues, J.; Duarte, P.; Nunes, D.; Costa, F.M.; Monteiro, T.; Martins, R.; Fortunato, E. Effect of solvents on ZnO nanostructures synthesized by solvothermal method assisted by microwave radiation: A photocatalytic study. *J. Mater. Sci.* **2015**, *50*, 5777–5787. [[CrossRef](#)]
4. Pimentel, A.; Ferreira, S.; Nunes, D.; Calmeiro, T.; Martins, R.; Fortunato, E. Microwave synthesized ZnO nanorod arrays for UV sensors: A seed layer annealing temperature study. *Materials* **2016**, *9*, 299. [[CrossRef](#)] [[PubMed](#)]

5. Pimentel, A.; Samouco, A.; Nunes, D.; Araújo, A.; Martins, R.; Fortunato, E. Ultra-fast microwave synthesis of ZnO nanorods on cellulose substrates for UV sensor applications. *Materials* **2017**, *10*, 1308. [[CrossRef](#)]
6. Kiazadeh, A.; Gomes, H.L.; Barquinha, P.; Martins, J.; Rovisco, A.; Pinto, J.V.; Martins, R.; Fortunato, E. Improving positive and negative bias illumination stress stability in parylene passivated IGZO transistors. *Appl. Phys. Lett.* **2016**, *109*, 051606. [[CrossRef](#)]
7. Bahubalindrani, P.G.; Martins, J.; Santa, A.; Tavares, V.; Martins, R.; Fortunato, E.; Barquinha, P. High-Gain transimpedance amplifier for flexible radiation dosimetry using ingazno tfts. *IEEE J. Electron Devices Soc.* **2018**, *6*, 760–765. [[CrossRef](#)]
8. Ide, K.; Nomura, K.; Hosono, H.; Kamiya, T. Electronic defects in amorphous oxide semiconductors: A review. *Phys. Status Solidi Appl. Mater. Sci.* **2019**, *1800372*, 1–28. [[CrossRef](#)]
9. Mancini, L.; Sala, S.; Recchioni, M.; Benini, L.; Goralczyk, M.; Pennington, D. Potential of life cycle assessment for supporting the management of critical raw materials. *Int. J. Life Cycle Assess.* **2015**, *20*, 100–116. [[CrossRef](#)]
10. Fernandes, C.; Santa, A.; Santos, Â.; Bahubalindrani, P.; Deuermeier, J.; Martins, R.; Fortunato, E.; Barquinha, P. A sustainable approach to flexible electronics with zinc-tin oxide thin-film transistors. *Adv. Electron. Mater.* **2018**, *4*, 1800032. [[CrossRef](#)]
11. Salgueiro, D.; Kiazadeh, A.; Branquinho, R.; Santos, L.; Barquinha, P.; Martins, R.; Fortunato, E. Solution based zinc tin oxide TFTs: The dual role of the organic solvent. *J. Phys. D Appl. Phys.* **2017**, *50*, 065106. [[CrossRef](#)]
12. Sun, S.; Liang, S. Morphological zinc stannate: Synthesis, fundamental properties and applications. *J. Mater. Chem. A* **2017**, *5*, 20534–20560. [[CrossRef](#)]
13. Baruah, S.; Dutta, J. Zinc stannate nanostructures: Hydrothermal synthesis. *Sci. Technol. Adv. Mater.* **2011**, *12*, 013004. [[CrossRef](#)] [[PubMed](#)]
14. Guo, R.; Guo, Y.; Duan, H.; Li, H.; Liu, H. Synthesis of orthorhombic perovskite-type ZnSnO<sub>3</sub> single-crystal nanoplates and their application in energy harvesting. *ACS Appl. Mater. Interfaces* **2017**, *9*, 8271–8279. [[CrossRef](#)] [[PubMed](#)]
15. Wu, J.M.; Chen, C.-Y.; Zhang, Y.; Chen, K.-H.; Yang, Y.; Hu, Y.; He, J.-H.; Wang, Z.L. Ultrahigh sensitive piezotronic strain sensors based on a ZnSnO<sub>3</sub> nanowire/microwire. *ACS Nano* **2012**, *6*, 4369–4374. [[CrossRef](#)] [[PubMed](#)]
16. Men, H.; Gao, P.; Zhou, B.; Chen, Y.; Zhu, C.; Xiao, G.; Wang, L.; Zhang, M. Fast synthesis of ultra-thin ZnSnO<sub>3</sub> nanorods with high ethanol sensing properties. *Chem. Commun.* **2010**, *46*, 7581. [[CrossRef](#)] [[PubMed](#)]
17. Lehnen, T.; Zopes, D.; Mathur, S. Phase-selective microwave synthesis and inkjet printing applications of Zn<sub>2</sub>SnO<sub>4</sub> (ZTO) quantum dots. *J. Mater. Chem.* **2012**, *22*, 17732. [[CrossRef](#)]
18. Lo, M.-K.; Lee, S.-Y.; Chang, K.-S. Study of ZnSnO<sub>3</sub>-nanowire piezophotocatalyst using two-step hydrothermal synthesis. *J. Phys. Chem. C* **2015**, *119*, 5218–5224. [[CrossRef](#)]
19. Mao, Y.; Park, T.-J.; Wong, S.S. Synthesis of classes of ternary metal oxide nanostructures. *Chem. Commun.* **2005**, 5721–5735. [[CrossRef](#)]
20. Choi, K.H.; Siddiqui, G.U.; Yang, B.; Mustafa, M. Synthesis of ZnSnO<sub>3</sub> nanocubes and thin film fabrication of (ZnSnO<sub>3</sub>/PMMA) composite through electrospray deposition. *J. Mater. Sci. Mater. Electron.* **2015**, *26*, 5690–5696. [[CrossRef](#)]
21. Li, Z.; Zhou, Y.; Bao, C.; Xue, G.; Zhang, J.; Liu, J.; Yu, T.; Zou, Z. Vertically building Zn<sub>2</sub>SnO<sub>4</sub> nanowire arrays on stainless steel mesh toward fabrication of large-area, flexible dye-sensitized solar cells. *Nanoscale* **2012**, *4*, 3490–3494. [[CrossRef](#)] [[PubMed](#)]
22. Kim, S.; Kim, H.; Janes, D.B.; Ju, S. Interface studies of N<sub>2</sub> plasma-treated ZnSnO nanowire transistors using low-frequency noise measurements. *Nanotechnology* **2013**, *24*, 305201. [[CrossRef](#)] [[PubMed](#)]
23. Nakayama, M.; Nogami, M.; Yoshida, M.; Katsumata, T.; Inaguma, Y. First-principles studies on novel polar oxide ZnSnO<sub>3</sub>; pressure-induced phase transition and electric properties. *Adv. Mater.* **2010**, *22*, 2579–2582. [[CrossRef](#)] [[PubMed](#)]
24. Dal Corso, A.; Posternak, M.; Resta, R.; Baldereschi, A. Ab initio study of piezoelectricity and spontaneous polarization in ZnO. *Phys. Rev. B* **1994**, *50*, 10715–10721. [[CrossRef](#)] [[PubMed](#)]
25. Datta, A.; Mukherjee, D.; Kons, C.; Witanachchi, S.; Mukherjee, P. Evidence of superior ferroelectricity in structurally welded ZnSnO<sub>3</sub> nanowire arrays. *Small* **2014**, *10*, 4093–4099. [[PubMed](#)]

26. Miyauchi, M.; Liu, Z.; Zhao, Z.-G.; Anandan, S.; Hara, K. Single crystalline zinc stannate nanoparticles for efficient photo-electrochemical devices. *Chem. Commun.* **2010**, *46*, 1529–1531. [[CrossRef](#)] [[PubMed](#)]
27. Lei, M.; Sheng, Y.; Wan, L.; Bi, K.; Huang, K.; Jia, R.; Liu, J.; Wang, Y. A novel self-catalytic route to zinc stannate nanowires and cathodoluminescence and electrical transport properties of a single nanowire. *J. Alloy. Compd.* **2016**, *657*, 394–399. [[CrossRef](#)]
28. Hwang, J.K.; Cho, S.; Dang, J.M.; Kwak, E.B.; Song, K.; Moon, J.; Sung, M.M. Direct nanoprinting by liquid-bridge-mediated nanotransfer moulding. *Nat. Nanotechnol.* **2010**, *5*, 742–748. [[CrossRef](#)]
29. Lim, T.; Kim, H.; Meyyappan, M.; Ju, S. Photostable Zn<sub>2</sub>SnO<sub>4</sub> nanowire transistors for transparent displays. *ACS Nano* **2012**, *6*, 4912–4920. [[CrossRef](#)]
30. Siddiqui, G.U.; Rehman, M.M.; Choi, K.H. Enhanced resistive switching in all-printed, hybrid and flexible memory device based on perovskite ZnSnO<sub>3</sub> via PVOH polymer. *Polymer* **2016**, *100*, 102–110. [[CrossRef](#)]
31. Yang, Y.J.; Rehman, M.M.; Siddiqui, G.U.; Na, K.H.; Choi, K.H. Effect of adding a polymer and varying device size on the resistive switching characteristics of perovskite nanocubes heterojunction. *Curr. Appl. Phys.* **2017**, *17*, 1733–1741. [[CrossRef](#)]
32. Wu, J.M.; Chen, K.-H.; Zhang, Y.; Wang, Z.L. A self-powered piezotronic strain sensor based on single ZnSnO<sub>3</sub> microbelts. *RSC Adv.* **2013**, *3*, 25184. [[CrossRef](#)]
33. Lee, K.Y.; Kim, D.; Lee, J.H.; Kim, T.Y.; Gupta, M.K.; Kim, S.W. Unidirectional high-power generation via stress-induced dipole alignment from ZnSnO<sub>3</sub> nanocubes/polymer hybrid piezoelectric nanogenerator. *Adv. Funct. Mater.* **2014**, *24*, 37–43. [[CrossRef](#)]
34. Wang, G.; Xi, Y.; Xuan, H.; Liu, R.; Chen, X.; Cheng, L. Hybrid nanogenerators based on triboelectrification of a dielectric composite made of lead-free ZnSnO<sub>3</sub> nanocubes. *Nano Energy* **2015**, *18*, 28–36. [[CrossRef](#)]
35. Wu, J.M.; Xu, C.; Zhang, Y.; Yang, Y.; Zhou, Y.; Wang, Z.L. Flexible and transparent nanogenerators based on a composite of lead-free ZnSnO<sub>3</sub> triangular-belts. *Adv. Mater.* **2012**, *24*, 6094–6099. [[CrossRef](#)] [[PubMed](#)]
36. Wu, J.M.; Xu, C.; Zhang, Y.; Wang, Z.L. Lead-free nanogenerator made from single ZnSnO<sub>3</sub> microbelt. *ACS Nano* **2012**, *6*, 4335–4340. [[CrossRef](#)] [[PubMed](#)]
37. Fu, X.; Wang, X.; Long, J.; Ding, Z.; Yan, T.; Zhang, G.; Zhang, Z.; Lin, H.; Fu, X. Hydrothermal synthesis, characterization, and photocatalytic properties of Zn<sub>2</sub>SnO<sub>4</sub>. *J. Solid State Chem.* **2009**, *182*, 517–524. [[CrossRef](#)]
38. Khan, M.N.; Jaisai, M.; Dutta, J. Photocatalytic inactivation of *Escherichia coli* using zinc stannate nanostructures under visible light. *Adv. Mater. Res.* **2015**, *1131*, 203–209. [[CrossRef](#)]
39. Zhao, Q.; Ju, D.; Song, X.; Deng, X.; Ding, M.; Xu, X.; Zeng, H. Polyhedral Zn<sub>2</sub>SnO<sub>4</sub>: Synthesis, enhanced gas sensing and photocatalytic performance. *Sens. Actuators B Chem.* **2016**, *229*, 627–634. [[CrossRef](#)]
40. Wang, Y.-T.; Chang, K.-S. Piezopotential-induced schottky behavior of Zn<sub>1-x</sub>SnO<sub>3</sub> nanowire arrays and piezophotocatalytic applications. *J. Am. Ceram. Soc.* **2016**, *99*, 2593–2600. [[CrossRef](#)]
41. Biswas, A.; Saha, S.; Jana, N.R. ZnSnO<sub>3</sub> nanoparticle-based piezocatalysts for ultrasound-assisted degradation of organic pollutants. *ACS Appl. Nano Mater.* **2019**, *2*, 1120–1128. [[CrossRef](#)]
42. Chen, Z.; Cao, M.; Hu, C. Novel Zn<sub>2</sub>SnO<sub>4</sub> hierarchical nanostructures and their gas sensing properties toward ethanol. *J. Phys. Chem. C* **2011**, *115*, 5522–5529. [[CrossRef](#)]
43. Singh, R.; Yadav, A.K.; Gautam, C. Synthesis and humidity sensing investigations of nanostructured ZnSnO<sub>3</sub>. *J. Sens. Technol.* **2011**, *1*, 116–124. [[CrossRef](#)]
44. Tharsika, T.; Haseeb, A.S.M.A.; Akbar, S.A.; Sabri, M.F.M.; Wong, Y.H. Gas sensing properties of zinc stannate (Zn<sub>2</sub>SnO<sub>4</sub>) nanowires prepared by carbon assisted thermal evaporation process. *J. Alloys Compd.* **2015**, *618*, 455–462. [[CrossRef](#)]
45. Pang, C.; Yan, B.; Liao, L.; Liu, B.; Zheng, Z.; Wu, T.; Sun, H.; Yu, T. Synthesis, characterization and opto-electrical properties of ternary Zn<sub>2</sub>SnO<sub>4</sub> nanowires. *Nanotechnology* **2010**, *21*, 465706. [[CrossRef](#)] [[PubMed](#)]
46. Chen, D.; Liu, Z.; Liang, B.; Wang, X.; Shen, G. Transparent metal oxide nanowire transistors. *Nanoscale* **2012**, *4*, 3001–3012. [[CrossRef](#)] [[PubMed](#)]
47. Shankar, K.S.; Raychaudhuri, A.K. Fabrication of nanowires of multicomponent oxides: Review of recent advances. *Mater. Sci. Eng. C* **2005**, *25*, 738–751. [[CrossRef](#)]
48. Ji, X.; Huang, X.; Liu, J.; Jiang, J.; Li, X.; Ding, R.; Hu, Y.; Wu, F.; Li, Q. Hydrothermal synthesis of novel Zn<sub>2</sub>SnO<sub>4</sub> octahedron microstructures assembled with hexagon nanoplates. *J. Alloys Compd.* **2010**, *503*, L21–L25. [[CrossRef](#)]

49. Zeng, J.; Xin, M.; Li, K.; Wang, H.; Yan, H.; Zhang, W. Transformation process and photocatalytic activities of hydrothermally synthesized Zn<sub>2</sub>SnO<sub>4</sub> nanocrystals. *J. Phys. Chem. C* **2008**, *112*, 4159–4167. [[CrossRef](#)]
50. Rovisco, A.; Branquinho, R.; Martins, J.; Oliveira, M.J.; Nunes, D.; Fortunato, E.; Martins, R.; Barquinha, P. Seed-layer free zinc tin oxide tailored nanostructures for nanoelectronic applications: Effect of chemical parameters. *ACS Appl. Nano Mater.* **2018**, *1*, 3986–3997. [[CrossRef](#)]
51. Su, B.; Wu, Y.; Jiang, L. The art of aligning one-dimensional (1D) nanostructures. *Chem. Soc. Rev.* **2012**, *41*, 7832. [[CrossRef](#)] [[PubMed](#)]
52. Christian, B.; Volk, J.; Lukàcs, I.E.; Sautieff, E.; Sturm, C.; Graillet, A.; Dauksevicius, R.; O'Reilly, E.; Ambacher, O.; Lebedev, V. Piezo-force and vibration analysis of ZnO nanowire arrays for sensor application. *Procedia Eng.* **2016**, *168*, 1192–1195. [[CrossRef](#)]
53. Fu, Y.; Nie, Y.; Zhao, Y.; Wang, P.; Xing, L.; Zhang, Y.; Xue, X. Detecting Liquefied Petroleum Gas (LPG) at room temperature using ZnSnO<sub>3</sub>ZnO nanowire piezo-nanogenerator as self-powered gas sensor. *ACS Appl. Mater. Interfaces* **2015**, *7*, 10482–10490. [[CrossRef](#)] [[PubMed](#)]
54. Xue, X.Y.; Chen, Y.J.; Wang, Y.G.; Wang, T.H. Synthesis and ethanol sensing properties of ZnSnO<sub>3</sub> nanowires. *Appl. Phys. Lett.* **2005**, *86*, 1–3. [[CrossRef](#)]
55. Wang, L.; Zhou, T.; Zhang, R.; Lou, Z.; Deng, J.; Zhang, T. Comparison of toluene sensing performances of zinc stannate with different morphology-based gas sensors. *Sens. Actuators B Chem.* **2016**, *227*, 448–455. [[CrossRef](#)]
56. Zhang, T.; Zhang, T.; Zhang, R.; Deng, J.; Lu, G.; Wang, L. Highly sensitive sensing platform based on ZnSnO<sub>3</sub> hollow cubes for detection of ethanol. *Appl. Surf. Sci.* **2017**, *400*, 262–268.
57. Najam Khan, M.; Al-Hinai, M.; Al-Hinai, A.; Dutta, J. Visible light photocatalysis of mixed phase zinc stannate/zinc oxide nanostructures precipitated at room temperature in aqueous media. *Ceram. Int.* **2014**, *40*, 8743–8752. [[CrossRef](#)]
58. Mali, S.S.; Su Shim, C.; Kook Hong, C. Highly porous Zinc Stannate (Zn<sub>2</sub>SnO<sub>4</sub>) nanofibers scaffold photoelectrodes for efficient methyl ammonium halide perovskite solar cells. *Sci. Rep.* **2015**, *5*, 11424. [[CrossRef](#)] [[PubMed](#)]
59. Siddiqui, G.U.; Rehman, M.M.; Choi, K.H. Resistive switching phenomena induced by the heterostructure composite of ZnSnO<sub>3</sub> nanocubes interspersed ZnO nanowires. *J. Mater. Chem. C* **2017**, *5*, 5528–5537. [[CrossRef](#)]
60. Cheng, B.; Ouyang, Z.; Chen, C.; Xiao, Y.; Lei, S. Individual Zn<sub>2</sub>SnO<sub>4</sub>-sheathed ZnO heterostructure nanowires for efficient resistive switching memory controlled by interface states. *Sci. Rep.* **2013**, *3*, 3249. [[CrossRef](#)] [[PubMed](#)]
61. Gou, H.; Zhang, J.; Li, Z.; Wang, G.; Gao, F.; Ewing, R.C.; Lian, J. Energetic stability, structural transition, and thermodynamic properties of ZnSnO<sub>3</sub>. *Appl. Phys. Lett.* **2011**, *98*, 1–4. [[CrossRef](#)]
62. Montenegro, D.N.; Hortelano, V.; Martínez, O.; Martínez-Tomas, M.C.; Sallet, V.; Muñoz-Sanjosé, V.; Jiménez, J. Non-radiative recombination centres in catalyst-free ZnO nanorods grown by atmospheric-metal organic chemical vapour deposition. *J. Phys. D Appl. Phys.* **2013**, *46*, 235302. [[CrossRef](#)]
63. Chen, Y.; Yu, L.; Li, Q.; Wu, Y.; Li, Q.; Wang, T. An evolution from 3D face-centered-cubic ZnSnO<sub>3</sub> nanocubes to 2D orthorhombic ZnSnO<sub>3</sub> nanosheets with excellent gas sensing performance. *Nanotechnology* **2012**, *23*, 415501. [[CrossRef](#)] [[PubMed](#)]
64. Song, P.; Wang, Q.; Yang, Z. Biomorphic synthesis of ZnSnO<sub>3</sub> hollow fibers for gas sensing application. *Sens. Actuators B Chem.* **2011**, *156*, 983–989. [[CrossRef](#)]
65. Wang, Y.; Gao, P.; Bao, D.; Wang, L.; Chen, Y.; Zhou, X.; Yang, P.; Sun, S.; Zhang, M. One pot, two phases: Individual orthorhombic and face-centered cubic ZnSnO<sub>3</sub> obtained synchronously in one solution. *Inorg. Chem.* **2014**, *53*, 12289–12296. [[CrossRef](#)] [[PubMed](#)]
66. Placke, A.; Kumar, A.; Priya, S. Synthesis and behavior of cetyltrimethyl ammonium bromide stabilized Zn<sub>1-x</sub>Sn<sub>x</sub>O<sub>3</sub> + x (0 ≤ x ≤ 1) nano-crystallites. *PLoS ONE* **2016**, *11*, e0156246. [[CrossRef](#)]
67. Bora, T.; Al-Hinai, M.H.; Al-Hinai, A.T.; Dutta, J. Phase transformation of metastable ZnSnO<sub>3</sub> upon thermal decomposition by in-situ temperature-dependent raman spectroscopy. *J. Am. Ceram. Soc.* **2015**, *98*, 4044–4049. [[CrossRef](#)]
68. Kumari, V.; Patra, A.K.; Bhaumik, A. Self-assembled ultra-small zinc stannate nanocrystals with mesoscopic voids via a salicylate templating pathway and their photocatalytic properties. *RSC Adv.* **2014**, *4*, 13626–13634. [[CrossRef](#)]

69. Saafi, I.; Dridi, R.; Mimouni, R.; Amlouk, A.; Yumak, A.; Boubaker, K.; Petkova, P.; Amlouk, M. Microstructural and optical properties of SnO<sub>2</sub>-ZnSnO<sub>3</sub> ceramics. *Ceram. Int.* **2016**, *42*, 6273–6281. [[CrossRef](#)]
70. Mary Jacqueline, M.; Justin Raj, C.; Jerome Das, S. Hydrothermal synthesis of highly crystalline Zn<sub>2</sub>SnO<sub>4</sub> nanoflowers and their optical properties. *J. Alloys Compd.* **2013**, *577*, 131–137. [[CrossRef](#)]



© 2019 by the authors. Licensee MDPI, Basel, Switzerland. This article is an open access article distributed under the terms and conditions of the Creative Commons Attribution (CC BY) license (<http://creativecommons.org/licenses/by/4.0/>).